cMiCE: a high resolution animal PET using continuous LSO with a statistics based positioning scheme ☆

Jinhun Joung[a,*], Robert S. Miyaoka[b], Thomas K. Lewellen[b]

[a] *Department of Advanced Research, Siemens Medical System, Nuclear Medicine Group, 2501 N. Barrington Rd., Hoffman Estates, IL 60195, USA*
[b] *Department of Radiology, University of Washington, Seattle, WA, USA*

Abstract

Objective: Detector designs for small animal scanners are currently dominated by discrete crystal implementations. However, given the small crystal cross-sections required to obtain very high resolution, discrete designs are typically expensive, have low packing fraction, reduced light collection, and are labor intensive to build. To overcome these limitations we have investigated the feasibility of using a continuous miniature crystal element (cMiCE) detector module for high resolution small animal PET applications. *Methods*: The detector module consists of a single continuous slab of LSO, $25 \times 25 \, mm^2$ in exposed cross-section and $4 \, mm$ thick, coupled directly to a PS-PMT (Hamamatsu R5900-00-C12). The large area surfaces of the crystal were polished and painted with TiO_2 and the short surfaces were left unpolished and painted black. Further, a new statistics based positioning (SBP) algorithm has been implemented to address linearity and edge effect artifacts that are inherent with conventional Anger style positioning schemes. To characterize the light response function (LRF) of the detector, data were collected on a coarse grid using a highly collimated coincidence setup. The LRF was then estimated using cubic spline interpolation. Detector performance has been evaluated for both SBP and Anger based decoding using measured data and Monte Carlo simulations. *Results*: Using the SBP scheme, edge artifacts were successfully handled. Simulation results show that the useful field of view (UFOV) was extended to $\sim 22 \times 22 \, mm^2$ with an average point spread function of $\sim 0.5 \, mm$ full width of half maximum ($FWHM_{PSF}$). For the same detector with Anger decoding the UFOV of the detector was $\sim 16 \times 16 \, mm^2$ with an average $FWHM_{PSP}$ of $\sim 0.9 \, mm$. Experimental results yielded similar differences between FOV and resolution performance. $FWHM_{PSF}$ for the SBP and Anger based method was 1.4 and 2.0 mm, uncorrected for source size, with a 1 mm diameter point source, respectively. *Conclusion*: A continuous detector module with an average $FWHM_{PSF}$ approaching one millimeter has been built and tested. Furthermore, the results demonstrate that our SBP scheme yields improved performance over traditional Anger techniques for our cMiCE detector. © 2002 Elsevier Science B.V. All rights reserved.

Keywords: Animal PET; Continuous LSO; PS-PMT; Positioning algorithm

1. Introduction

Animal PET imaging plays a key role in evaluating whether a new radiopharmaceutical

can be used to successfully visualize the desired physiological or biochemical parameter for which it was designed [1]. With the advent of new ultra-high resolution (approaching 1 mm spatial resolution) PET detector systems, the role of small animal PET imaging will continue to expand.

Many research groups have been involved in developing different types of animal PET systems [2–8]. Among those efforts, most designs have consisted of detectors assembled using tiny discrete crystal elements identified by position sensitive or multi-anode photomultiplier tubes (PMT). This is because the desired spatial resolution can be achieved by selecting the size of the crystal element. For small animal systems crystals with dimensions of <2 mm are typical. However, as described in detail by Siegel [6], making the crystals narrower for higher resolution causes several problems including inter crystal scatter, light collection difficulty, practical difficulties of accurate and consistent crystal size, and high cost associated with fine crystal cutting and treatment.

There have been several previous efforts looking at using a continuous crystal for small animal PET applications [6,9]. However, the investigations were conducted superficially at the middle of the detector and the edge effect artifacts (i.e., event overlap, spatial resolution degradation and the FOV shrinkage at the edge) that are the main obstacles in continuous crystal detector design were not addressed in detail.

The feasibility of using a continuous crystal detector for high resolution animal PET imaging has been investigated aiming to reduce the system cost; to improve the system performance; and to increase the system's sampling density without requiring detector motion. Further, a new statistics based positioning (SBP) algorithm has been implemented to address linearity and edge effect artifacts that are inherent with conventional Anger style positioning schemes.

In this investigation, we describe the theory of the SBP algorithm and provide results comparing the performance characteristics of an ultra-high resolution continuous crystal PET detector using our SBP algorithm versus conventional Anger techniques.

2. Theory: statistics based positioning algorithm

Suppose, the *parent distribution* of observing PMT outputs $M = M_1, M_2, \ldots, M_n$ for scintillation position x, are independent Gaussian with mean, μ, and standard deviation σ.

The probability for making any single observation m_i from the parent distribution M_i given x is

$$P_i[m_i|x] = \frac{1}{\sigma_i(x)\sqrt{2\pi}}\exp\left(-\frac{(m_i - \mu_i(x))^2}{2\sigma_i^2(x)}\right). \quad (1)$$

Considering the entire set of n independent observations for each channel, the probability of observing a particular set is given by the product of the individual probability functions:

$$P[m_1, m_2, \ldots, m_n|x] = \prod_{i=1}^{n} P_i[m_i|x]. \quad (2)$$

The log of Eq. (2) reduces to

$$\ln P = -\left(\sum_{i=1}^{n} \frac{(m_i - \mu_i(x))^2}{2\sigma_i^2(x)} + \sum_{i=1}^{n} \ln \sigma_i(x)\right). \quad (3)$$

Thus, the maximum likelihood solution is achieved by minimizing the quantity inside of the bracket in Eq. (3). In addition, we have determined through experiment that the second term of Eq. (3) does not effect the estimation accuracy.

Finally, the estimate of the event position is determined by

$$\hat{x} = \arg_{\forall x} \min_{x=\hat{x}} \left(\frac{(m_i - \mu_i(x))^2}{\sigma_i^2(x)}\right). \quad (4)$$

Note that, the Gaussian model, unlike the Poisson model, frees the estimator from the constraint that the variance must follow the mean.

3. Materials and methods

3.1. Implementation overview

An overview of the implementation strategy of the proposed algorithm is illustrated in Fig. 1. The implementation follows a machine learning approach. It is also can be regarded as a classification problem, i.e., given a training sequence of examples, figure out if a new example belongs to the set
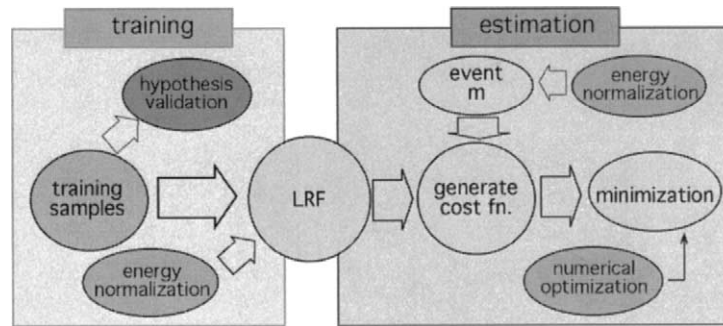
Fig. 1. Graphical representation of the implementation overview.

or not. In the training phase, the light response function (LRF) is estimated from the training samples after going through Gaussian fitting and a cubic spline interpolation process. All hypotheses that support the estimation theory were validated in this phase.

Once the LRF, the true statistical characteristics of a given detector as a function of position, is estimated with a desired search resolution, the predicted event position is determined in which the cost function, i.e., the discrepancy between the LRF and a given event, is minimized. Numerical optimization methods such as event localization and a hierarchical step search were employed to speed up the minimization process. Employing an energy normalization also enables the estimator to be energy independent. The function of each component is explained in detail in the following sub-sections.

3.2. Hypothesis validation

The SBP algorithm was derived under the assumption that the photon distribution of each channel for a given position is independent and Gaussian. Experimental data were empirically analyzed to prove this hypothesis. A population of 2×10^5 events were collected at the middle of the detector. The goodness of the Gaussian fit of each channel output was validated by examining the discrepancy between the data distribution and a Gaussian curve fit to the data. The dependency between channels was evaluated by computing the linear correlation coefficient. In general, zero correlation does not imply statistical independence; however, it does in the Gaussian case. Since all 12 channels are utilized for event estimation, the sample mean of the correlation coefficients between channels was considered as a dependency validation metric defined as

$$\bar{\rho}_{dep} = \arg_{i \neq j} \frac{1}{n(n-1)} \sum_{i=1}^{n} \sum_{j=1}^{n} |\rho(i,j)| \qquad (5)$$

where $\rho(i,j)$ is a linear correlation coefficient between the ith and jth channel.

3.3. Monte Carlo simulation

Monte Carlo simulation studies were conducted to predict the characteristics of the module and to evaluate the SBP scheme under ideal conditions (i.e., all photon interactions were photoelectric and occurred at the same interaction depth).

A Monte Carlo simulation program, 'DETECT' [10], was used to simulate photon transport through a detector assembly. All simulation parameters and conditions were specified to mimic our experimental continuous miniature crystal element (cMiCE) detector module.

The detector module assembly, illustrated in Fig. 2, was simulated to consist of a single slab of lutetium oxy orthosilicate, LSO(Ce), $25 \times 25 \, mm^2$ in exposed cross-section and 4 mm thick, coupled directly to a $6+6$ cross-anode position sensitive-PMT (Hamamatsu R5900-00-C12). The large area surfaces of the crystal were simulated as polished and painted with TiO_2. To reduce edge effects the
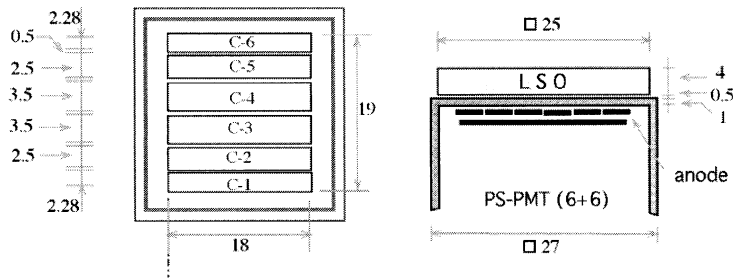
Fig. 2. Position sensitive PMT (Hamamatsu, R5900-00-C12) anode layout and detector module configuration.

short surfaces of the crystal were left unpolished and painted black. The depth of interaction of the scintillation position was fixed at the middle (2 mm depth) of the LSO slab. The quantum efficiency of the PMT was set to be 0.25 [11].

3.4. Experimental configuration

Experimental studies were conducted with a module as described in Fig. 2. The LSO crystal is illustrated in Fig. 3. Since the LSO material is naturally radioactive, a coincidence detection circuit was built in addition to mechanical collimation to eliminate the LSO background ($\sim$700 cps). The collimator is a triple 'slot' arrangement with one 7.5 cm thick and two 2.5 cm thick lead blocks with 5, 2 and 1 mm diameter holes, respectively. The slots of the collimator ware separated by 6.5 and 4.5 cm center to center as shown in Fig. 2. A ^{68}Ge source ($\sim$0.25 mCi) was placed in the center of the 7.5 cm thick lead block. The coincidence detector module consists of a $4 \times 8 \times 20$ mm^3 MLS crystal coupled to one side of a dual photocathode PMT (Hamamatsu R1548). The detector was placed directly in front of the 5 mm diameter hole. This guaranteed that the solid angle to the coincidence detector was greater that the solid angle to the cMiCE detector. The imaging detector was placed on a translation device (Fig. 4) that could move along both the $x-$ and $y-$axis. By moving the imaging detector the collimated 511 keV flux could be positioned at any location on the face of the detector module.
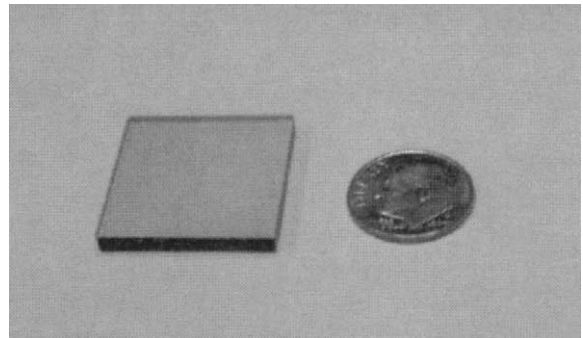

Fig. 3. LSO crystal ($25 \times 25 \times 4$ mm^3) with a dime.

3.5. Coincidence acquisition system

The coincidence acquisition system and signal flow is illustrated in Fig. 6. Both the imaging and coincidence detector modules processing units are identical except a summing circuit is added for the imaging detector. Each of the 12 channels (6 + 6 channels) of the imaging detector is directly fed into an analog to digital converter (ADC, LeCroy FERA 4300B). The 6 x-channels are branched into a 6-ch variable amplifier (LeCroy 612AM) and then summed. The summed x-signal is transmitted to the coincidence detection unit (LeCroy 622) via a timing filter amplifier (TFA, Ortec 454), constant fraction discriminator (CFD, Tennelec TC453) and a delay (Tennelec, TC412A). The signal from the coincidence detector was fed to a preamplifier (NPL, 113). After the preamplifier it followed a similar signal path as the summed signal from the imaging detector (Fig. 5).
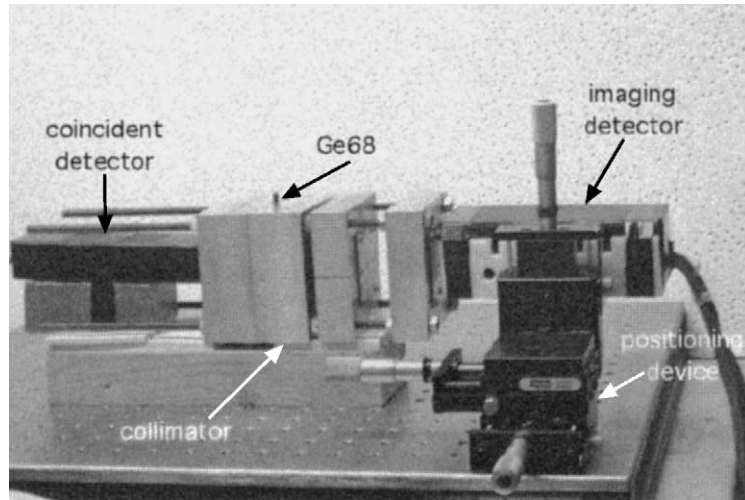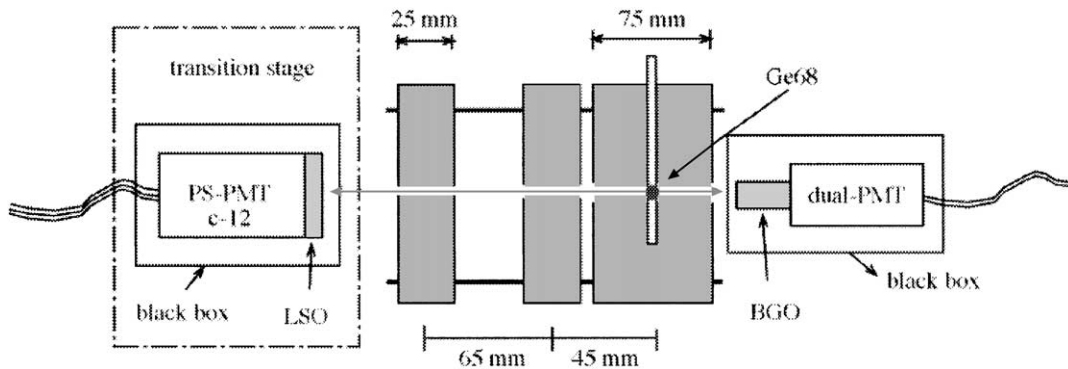
Fig. 4. Experimental configuration.

Fig. 5. Mechanical collimator dimensions and coincidence detection configuration.

The TFA module is used to shape pulses and set the size of the signal being sent to the CFD unit. The module provides continuously adjustable gain (X2–X250). The CFD accepts signals in the 0 to −5 V ranges and generates fast negative or positive timing output signals.

The delay module performs the delay of analog signals in 1 ns increments from 0 to 63 ns. It is used to align the two fast timing signals from the imaging and coincidence detectors.

The quad coincidence module provides the logic functions for coincidence detection.

The gate/delay generator generates the gate pulse to trigger the ADC module.

Whenever the ADC unit is triggered by the gate/delay generator, all 12 signals (6 + 6 channels) are digitized and stored to a buffer memory (Kinetics system 3982). After the buffer fills the data are transferred to the processing computer (Macintosh G4). A diagram of the coincidence detection components configuration and signal flow is illustrated in Fig. 6.

3.6. Light response function (LRF) estimation

The SBP algorithm requires prior knowledge of the detector response (characteristics) as a function of event position. Characterizing the detector
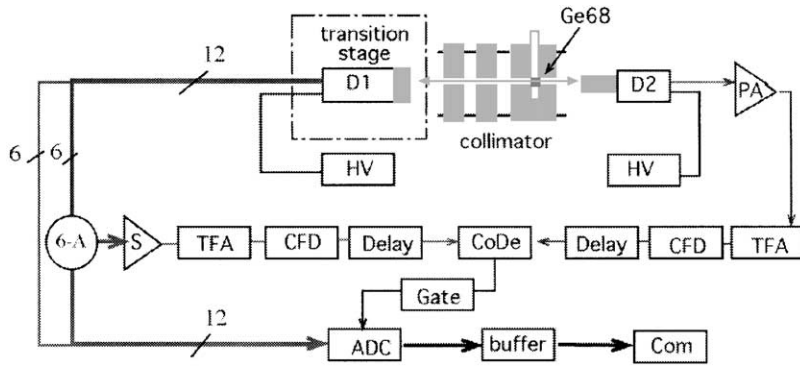
Fig. 6. Acquisition system layout: main components and signal flow.

response function (i.e. mean and variance as a function of position) for a detector can be determined by a parametric or non-parametric method [12]. For the PS-PMT based system application, a non-parametric method such as interpolation is more suitable. This is because the shape of the two-dimensional (2D) LRF distribution is not isotropic due to the rectangular shape of the anode. A parametric method is more suitable for isotropic LRF estimation. An additional advantage of the non-parametric approach is the fact that it is more flexible to handle PMT output fluctuations at the edge of the detector caused by the reflected photons.

Traditionally, the LRFs are determined experimentally by moving a point or line source on a known grid with the desired precision and observing each PMT response as a function of source position. However, this process is not only labor intensive but also limited by noise and the precision of the measurements.

In our investigation, the LRFs were generated using two estimation processes; Gaussian fitting and Cubic spline interpolation. The benefits of modeling the LRF are two-fold. First, it is convenient to estimate the LRF with the desired search resolution. Second, it is more robust under statistical noise when the derivative of the LRF is involved [13].

Gaussian fitting is performed to extract the mean and variance information from the training data set (see Fig. 7). Once the Gaussian fitting process is done, cubic spline interpolation is used.

The cubic spline interpolation is applied to a coarse set of LRF samples to estimate the LRF with the desired search resolution as shown in Fig. 8. We used a 10:1 interpolation versus sample ratio. For example, 1 cm space sampling was used to generate a 1 mm precision LRF. The cubic spline function provides smooth first order and continuous second order derivatives of the LRF. Thus, a smooth LRF is guaranteed. The smoothness of the LRF is important when the derivative or Hessian function of the LRF is needed for further numerical optimization.

3.7. Energy normalization

The proposed SBP method includes an energy normalization feature to make it energy independent. This normalization technique improves the spatial resolution performance especially at the edge of the detector, where the energy height collection efficiency is poorer than toward the middle of the detector.

The normalized PM energy E_i is

$$\tilde{E}_i = k\frac{E_i}{\sum_{i=1}^{n} E_i} \tag{6}$$

where the denominator term is total energy for a given event and k is a fixed scale factor that makes the PM signal an integer value for computational convenience. However, this process might change the conditional independence among the normalized measurements.
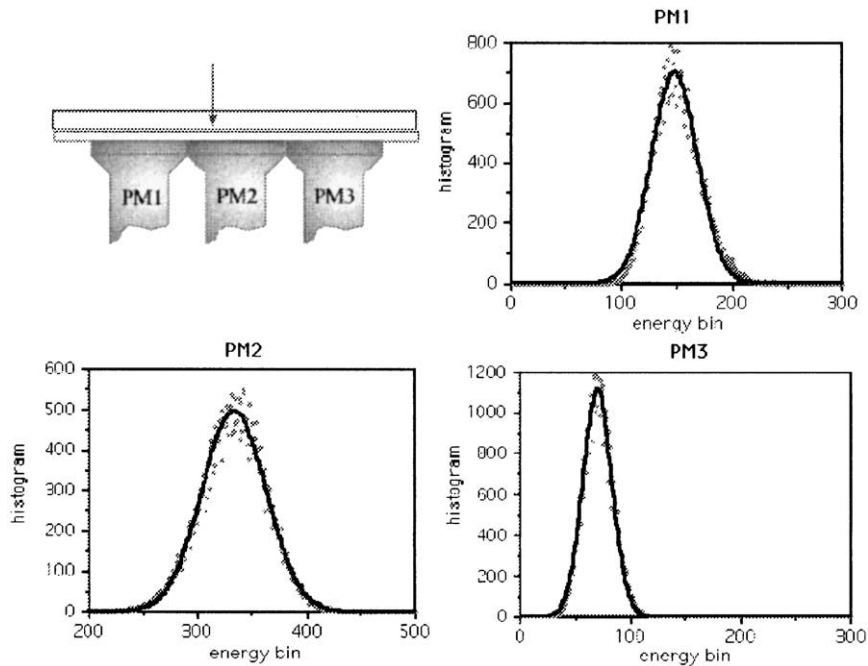
Fig. 7. Gaussian fitting process example. An arrow in top left figure represents event location.

3.8. Computational requirement

Solving the computational requirement is one of the biggest challenges for practical implementation of the proposed algorithm. In order to reduce the computational requirement for the proposed SBP method, an event localization and hierarchical step search method was developed. The methods are illustrated in Fig. 7. Event localization is achieved by constraining the search area based on an initial guess of the event location. The size of the search area is then reduced using a hierarchical step search technique. These steps are done iteratively until the desired pixel resolution is achieved.

Computational feasibility of the proposed method was also reviewed in terms of memory requirement and execution time considering the localization and the step search method.

3.9. Linearity correction

Since the linearity distortion for Anger based positioning methods can be quite severe, it is necessary to determine the spatial resolution after linearity correction for an appropriate comparison between the spatial resolution performance of Anger based methods and the proposed SBP method. Since our SBP method is unbiased, linearity correction is only required for the Anger positioning scheme.

To compute the expected spatial resolution after linearity correction, the degree of distortion from the true event location is determined using a third-order polynomial curve fit. Since the full 2D linearity correction is outside the scope of this investigation, a 1D linearity correction is applied to simplify the problem. A 1D correction should provide a reasonable approximation of how the spatial resolution changes after linearity correction.

4. Results

4.1. Hypothesis validation

An example of the graphical representation of the dependency between channels along with the
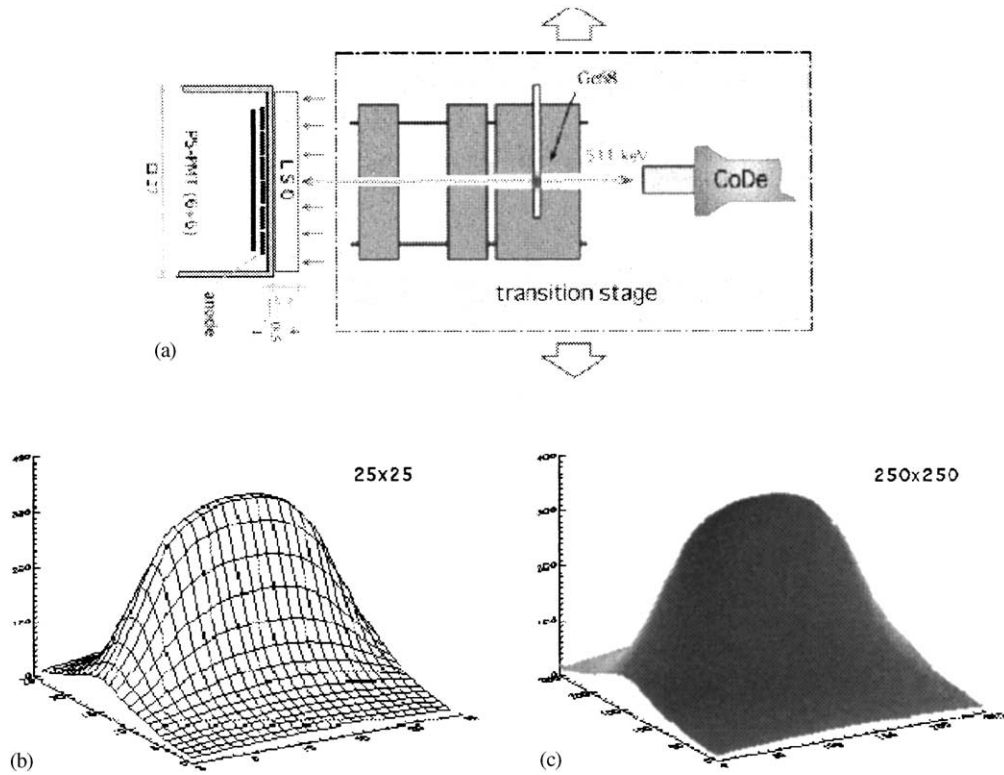
Fig. 8. Cubic spline interpolation example: (a) Coarse LRF samples: graphical illustration of sample LRF generation process; (b) 25×25 2D LRF samples and (c) interpolated LRF 250×250 w/0.1 mm search resolution.
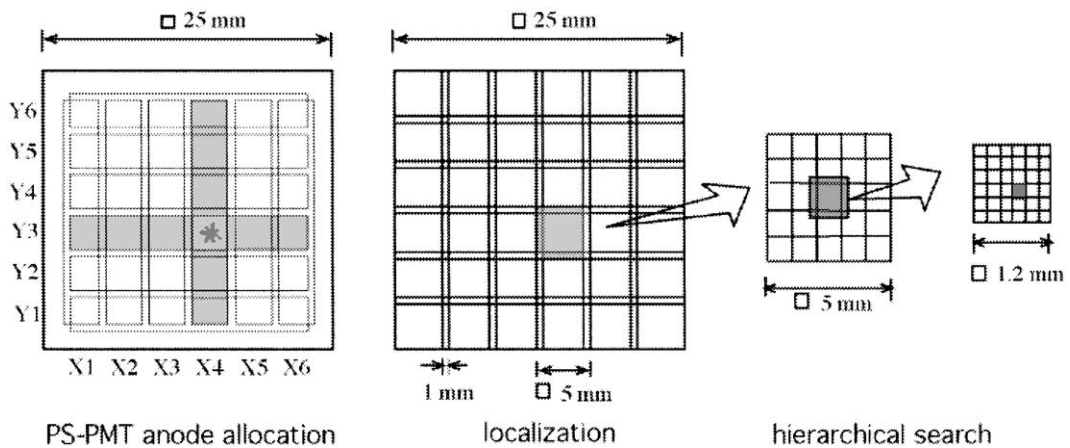

Fig. 9. Speed up techniques: Event localization constrains search area based on maximum x and y channels. Search area is constrained inside of 5×5 mm^2 gray box shown in above example. Hierarchical step search is then employed. Search step changes from coarse to fine and search area gets smaller during hierarchical step search.
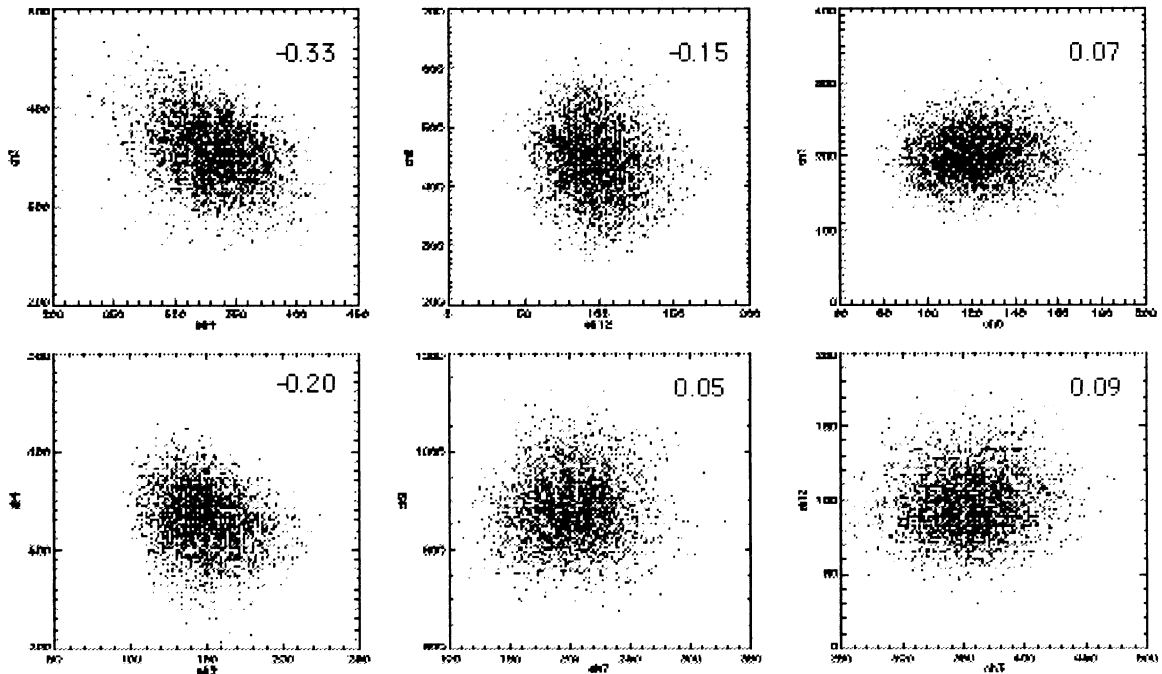
Fig. 10. Examples of channel dependency. Graphical representation of channel dependencies shown from the top left ch3:ch2, ch8:ch12, ch7:ch5, ch4:ch2, ch9:ch7 and ch12:ch3. 200 K events were detected at the middle of a detector.

correlation coefficient for events (200 K) detected at the middle of detector are illustrated in Fig. 10. The sample mean of the correlation coefficient (see Eq. (5)) is 0.16. This result indicates that there exists a slight correlation between channels but the dependency may not be a significant factor for the estimation performance. The goodness of the Gaussian fit is also graphically provided in Fig. 11. Results shows a high correlation (~ 0.99) between the Gaussian fit and the measured data for every channel.

4.2. Computational review

A total of ~ 432 Mbytes is required for the LRF lookup table generation. This requirement was estimated based on the following considerations: 2D implementation; number of channels per module is 12 (i.e., $6 + 6$); 12 neighbor PMTs per PMT; area covered by a single channel is 25×125 (search resolution $= 0.2$ mm); number of modules per ring is 24; number of rings of system is 5; the

precision of LRF lookup table is 4 bytes; and two tables are needed for mean and variance lookup (i.e., $12 \times 12 \times 25 \times 125 \times 24 \times 5 \times 4 \times 2$).

Execution time was estimated for two general-purpose computers, an Apple power Macintosh G4 (400 MHz CPU w/1 Mbyte 2-level cache) and a Compaq Alpha system (375 MHz CPU w/8 M byte 3-level cache). Event localization (see Fig. 9) and fast search techniques such as iterative alternating estimation (solving two separate independent 1D problems) and hierarchical fast search were considered to minimize the search area and points. Based on the above considerations, 100 search points with 12 PMTs per event computation were considered. Execution times of 130 and 24 μs per event were required for the Macintosh and Alpha system, respectively.

4.3. Simulation results

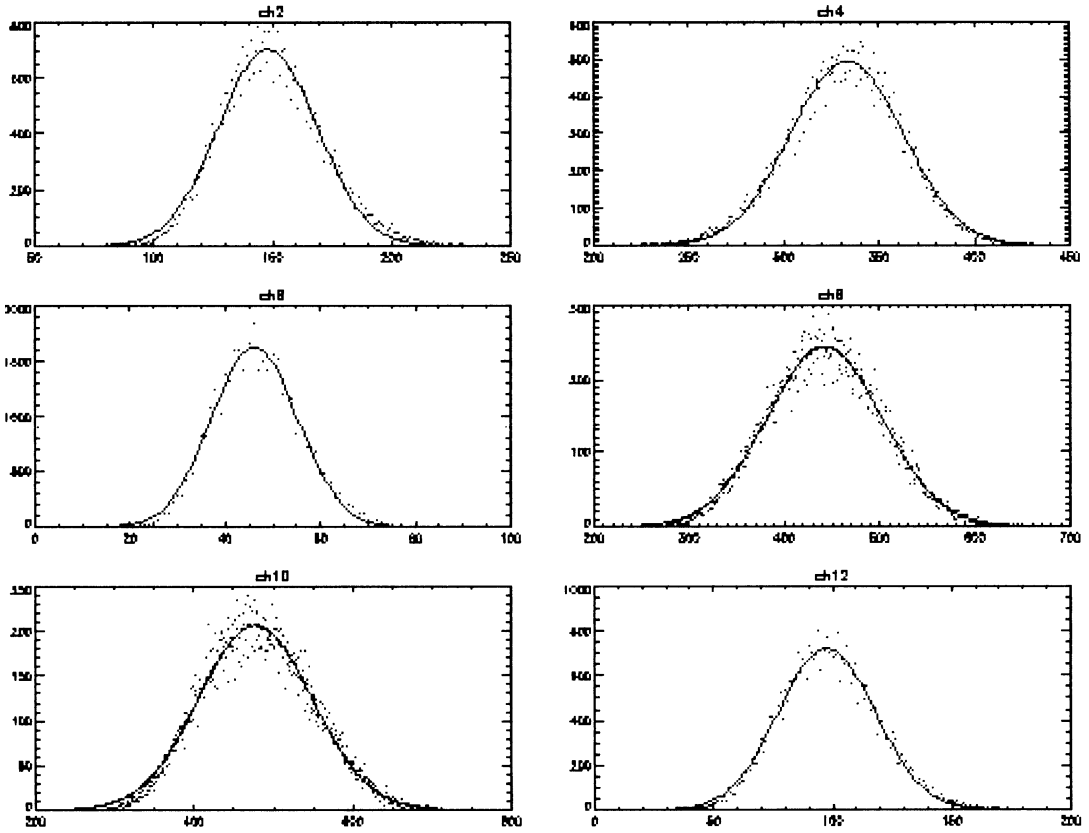The linearity performances of the SBP method and Anger positioning are graphically represented

Fig. 11. The goodness of Gaussian fit. Correlation coefficient between Gaussian fit and measured data was ∼0.99 for each channel.
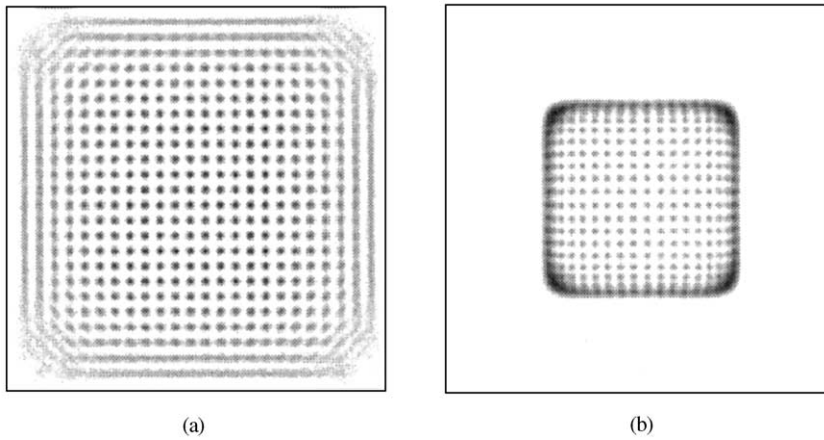

(a)   (b)

Fig. 12. Simulation results. (a) SBP method: UFOV can be extended up to $22 \times 22 \, mm^2$. Average $FWHM_{PSF}$ was ∼0.5 mm. (b) Anger based method: edge effect artifacts were quite severe. Events were overlapped beyond 16×16 FOV boundary. Average $FWHM_{PSF}$ was ∼0.9 mm.

in Fig. 12. 24 × 24 evenly spaced points on a 25 × 25 mm^2 crystal were selected as test points with DOI fixed at 2 mm from the entrance face of the crystal. Two thousand events were collected at each test point. The SBP results show non-biased performance. On the other hand, edge effect artifacts were quite severe in the Anger. Fig. 13 shows a profile across the central row of each image from Fig. 12. The SBP method was able to decode all 24 points while the Anger based method

decoded 16 points. The useful field of view (UFOV) of the SBP method was ∼22 × 22 mm^2 with an average point spread function (PSF) of 0.5 mm full width of half maximum (FWHM$_{PSF}$). For the same detector with Anger decoding the UFOV of the detector was ∼16 × 16 mm^2 with an average FWHM$_{PSF}$ of 0.9 mm.

A linearity correction curve along with a profile of the central row of test points before and after linearity correction is illustrated in Fig. 14(a). The
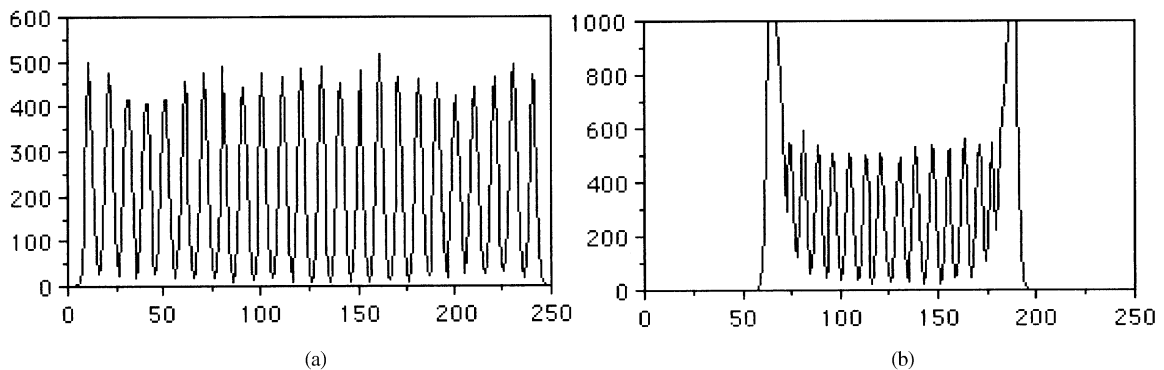

Fig. 13. Profiles for the middle row test points. (a) SBP method and (b) Anger method.
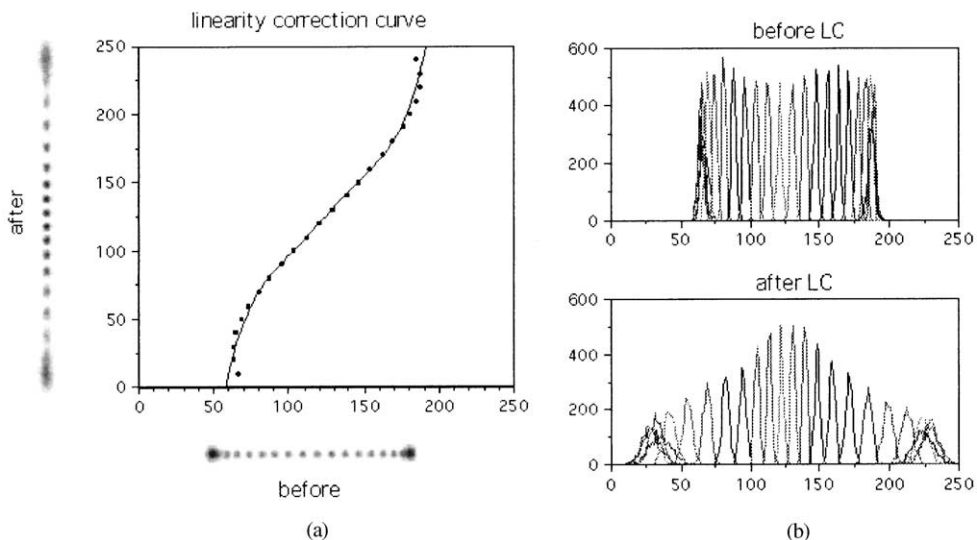

Fig. 14. Linearity correction effects (simulation). (a) Linearity correction curve and (b) point spread function profile. Spatial resolution and uniformity is degraded as moving toward the edge of the detector.
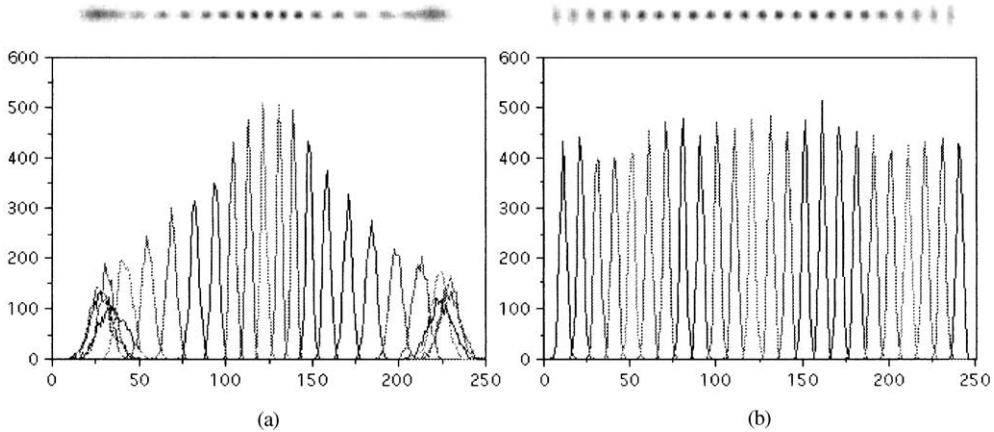
Fig. 15. PSF performance comparison (simulation). (a) Anger method (linearity corrected) and (b) SBP method.

point spread function of the central row is shown in Fig. 14(b). The spatial resolution and non-uniformity of the PSF increases toward the edge of the detector. Furthermore, the test points beyond the $16 \times 16\,mm^2$ UFOV were not recovered even after linearity correction.

The PSF versus position along one axis of the crystal is plotted for both methods in Fig. 15. The Anger results are after linearity correction. The $FWHM_{PSF}$ was computed by multiplying the square root of the variance by 2.35. The variance of each PSF was computed based on a Gaussian curve fit. On average the spatial resolution for the SBP method is 44% better than the Anger method along. It also provides better spatial uniformity and linearity (Fig. 16).
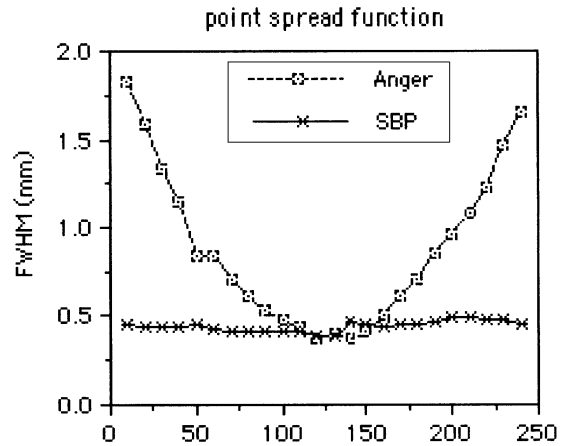
4.4. Experimental results

Experimental results of the linearity performance of the SBP and Anger methods are shown in Fig. 17. Eight–five, 7×7 plus 6×6, evenly spaced test points were used (see Fig. 17(a)). Eleven test points, along the middle of the detector, with 2 mm spacing were selected and evaluated. FOV shrinkage and edge effects were observed using Anger positioning.

The same evaluation procedures applied to the simulation results were conducted on the experimental results. Linearity correction was performed on the Anger results as described earlier and the

Fig. 16. $FWHM_{PSF}$ (simulation). SBP has an average of $\sim 0.5\,mm$ $FWHM_{PSF}$ while Anger method has $\sim 0.9\,mm$ $FWHM_{PSF}$.

results are shown in Fig. 18. The experimental results show good agreement with the simulation findings. The UFOV of the SBP method was at least $20 \times 20\,mm^2$ with an average point spread function of 1.4 mm while the Anger method provided a $16 \times 16\,mm^2$ UFOV with an average $FWHM_{PSF}$ of 2.0 mm.

Profiles of the point spread functions and the FWHM of point spread functions are illustrated in Figs. 19 and 20, respectively. Note that the diameter of the point source was $\sim 1\,mm$ and the $FWHM_{PSF}$ values are provided without correcting for the size of the point source.
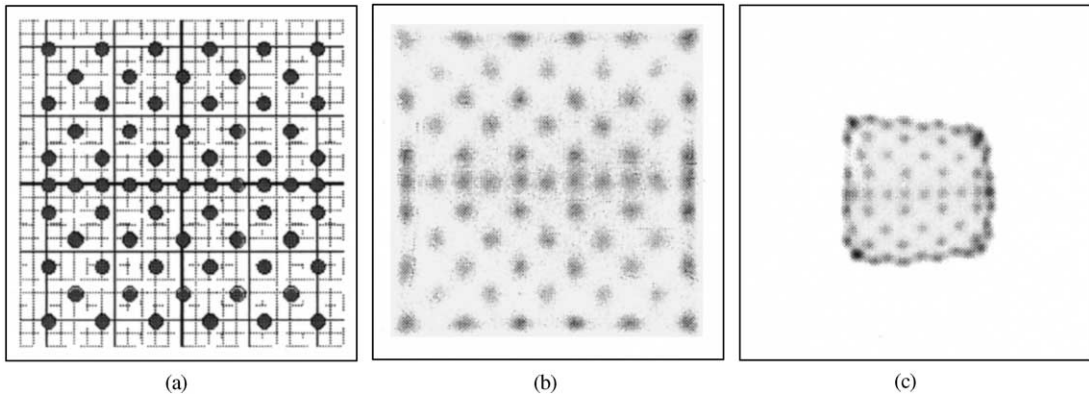
Fig. 17. Experimental results. (a) Grid of test points, (b) SBP results and (c) Anger result.
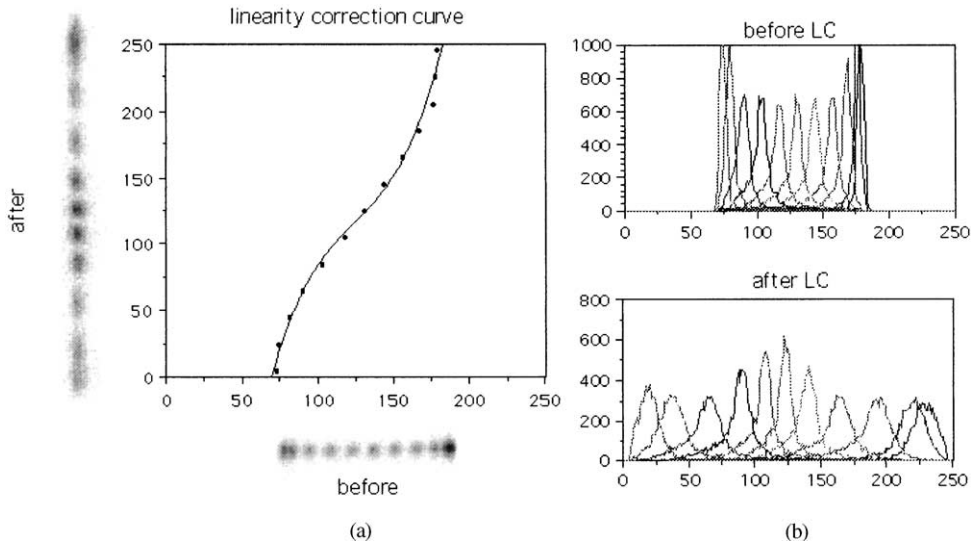

Fig. 18. Linearity correction effects (experiment) (a) linearity correction curve and (b) point spread function profile.

5. Discussion and conclusion

At the edge of the detector the shape of the LRF function changes abruptly. Consequently, finer samples are required for accurate interpolation of the LRF at the edge. However, in this investigation, the training samples for the LRF estimation were collected using a coarse grid within a $20 \times 20 \, \text{mm}^2$ FOV as shown in Fig. 18(a). There-

fore, the LRF was inaccurately estimated at the edge of the crystal due to the coarse sampling and the absence of samples outside of a $20 \times 20 \, \text{mm}^2$ FOV. As a result, profiles of edge test points are squeezed as shown in Figs. 19(b) and 20. The FWHM$_{PSF}$ values for experimental studies were provided without correction of point source size and computed based on a Gaussian curve fit to the measured point spread function. Since the total
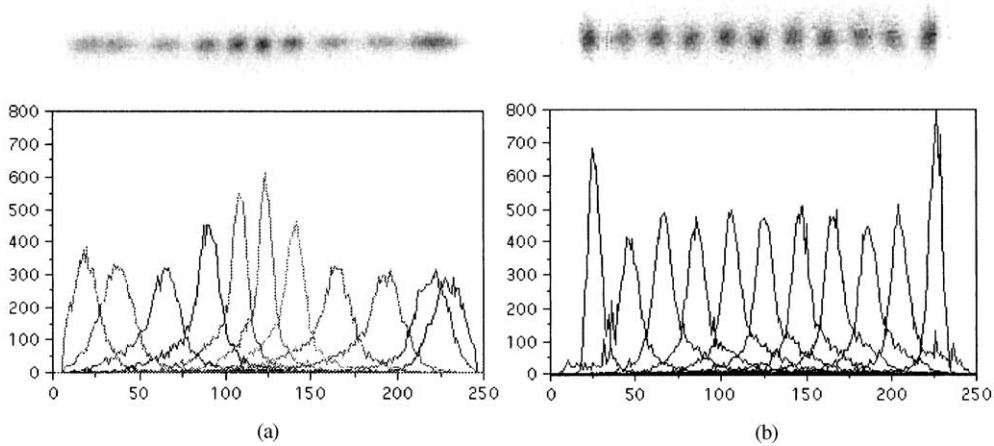
Fig. 19. PSF performance comparison (experiment). (a) Anger method (linearity corrected) and (b) SBP method. Note that the events falling outside of 0 and 250 were truncated in (a).
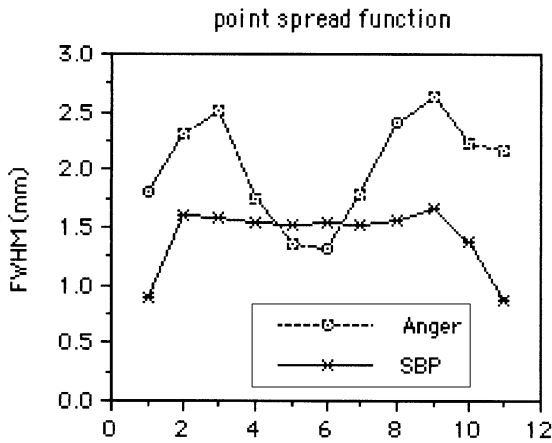

Fig. 20. FWHM$_{PSF}$ (experiment). SBP has an average of ~ 1.4 mm FWHM$_{PSF}$ while Anger method has ~ 2.0 mm FWHM$_{PSF}$.

count per each test point was not large, there might be small errors associated with the accuracy of the curve fitting process.

The proposed module excludes a light guide. This may or may not affect the overall performance when using Anger style positioning techniques. In general, a light guide will reduce the linearity distortion; however, it also tends to reduce spatial resolution. On the other hand, it is unlikely that the use of a light guide would improve the edge performance using Anger positioning.

Simulation (experimental) results show that the proposed SBP method has $\sim 90(56)\%$ and $\sim 44(30)\%$ improvement over conventional Anger positioning in terms of UFOV extension and FWHM$_{PSF}$, respectively.

Our computational review indicates that the proposed algorithm is feasible if numerical optimization techniques, i.e., event localization and hierarchical step search, are implemented. The execution time could be reduced further by using faster CPUs and/or parallel processing with dedicated processors.

The benefits of using the proposed SBP method over conventional methods, such as Anger, for small scintillation system applications are fourfold: (1) field of view extension; (2) elimination of edge effect artifacts; (3) spatial resolution improvement and (4) more uniform spatial resolution performance.

The advantages of using the proposed continuous module with the SBP scheme rather than the discrete crystal element module are as follows: (1) lower cost of the detector module; (2) less labor intensive to build; (3) better light collection efficiency; (4) continuous sampling and (5) DOI feature extension capability. One bit of DOI information can easily be implemented by adding

an additional crystal layer with its own LRF lookup table.

The results illustrate that low cost, very high resolution small animal PET systems are feasible. The key to significantly reducing the costs of ultra-high resolution detector designs was the development of our SBP algorithm that can be used with continuous crystal detector designs.

References

[1] R. Hichwa, J. Nucl. Med. 35 (8) (1994) 1396.

[2] A. Chatziioannou, R.W. Silverman, K. Meadors, T.H. Farquhar, S.R. Cherry, IEEE Trans. Nucl. Sci. 47 (2.) (2000) 422.

[3] S.R. Cherry, S. Siegel, A.R. Ricci, L. Eriksson, E.J. Hoffman, M.E. Phelps, Nucl. Instr. and Meth. in Phys. Res. A 348 (1994) 612.

[4] S.R. Cherry, et al., IEEE Trans. Nucl. Sci. 44 (3) (1997) 1161.

[5] R.S. Miyaoka, S.G. Kohlmyer, T.K. Lewellen, IEEE Trans. Nucl. Sci. (2001), in press.

[6] S. Siegel, S.R. Cherry, A.R. Ricci, Y. Shao, M.E. Phelps, IEEE Trans. Nucl. Sci. 42 (4) (1995).

[7] J.J. Vaquero, J. Seidel, S. Siegel, W.G. Gandler, M.V. Green, IEEE Trans. Med. Imaging 17 (6) (1998).

[8] M. Watanabe, et al., IEEE Trans. Med. Imaging 11 (4) (1992) 577.

[9] J. Seidel, W.R. Gandler, M.V. Green, IEEE Trans Nucl. Sci. 43 (3) (1996) 1968.

[10] G.F. Knoll, T.F. Knoll, T.M. Henderson, IEEE Trans. Nucl. Sci. NS-35 (1988) 872.

[11] J.S. Karp, G. Muehllehner, Phys. Med. Biol. 30 (1985) 643.

[12] J. Joung, R.S. Miyaoka, S.G. Kohlmyer, T.K. Lewellen, IEEE Trans. Nucl. Sci. (2001), in progress.

[13] J. Joung, R.S. Miyaoka, S.G. Kohlmyer, T.K. Lewellen, IEEE Trans. Nucl. Sci. 47 (2000) 1104.